Article

Novel Magnetic Silica-Ionic Liquid Nanocomposites for Wastewater Treatment

Ayman M. Atta [1],* , Yaser M. Moustafa [2], Abdelrahman O. Ezzat [1] and Ahmed I. Hashem [3]

[1] Chemistry Department, College of Science, King Saud University, Riyadh 11451, Saudi Arabia; ao_ezzat@ksu.edu.sa
[2] Egyptian Petroleum Research Institute, Nasr City 11727, Cairo, Egypt; ymoustafa12@yahoo.com
[3] Chemistry Department, College of Science, Ain Shams university, Abasia 11566, Cairo, Egypt; emyhashem2004@yahoo.com
* Correspondence: aatta@ksu.edu.sa

check for updates

Abstract: In this work, new imidazolium silica-ionic liquids doped with magnetite nanocomposites are prepared for use in the field of water purification owing to their unique properties, which can be manipulated by an external magnetic field. A silane precursor based on aminopropyltriethoxysilane (APTS) condensed with *p*-hydroxybenzaldehyde and glyoxal in an acetic acid solution is used to prepare disiloxyimidazolium ionic liquid (SIMIL). The silica composite (Si-IL) and silica-coated magnetite (Fe_3O_4-Si-IL) composites are prepared using the sol-gel technique. The chemical structures, morphologies, crystalline lattice structures, thermal stabilities, surface charges, surface areas, particle sizes, and magnetic characteristics of Fe_3O_4-Si-IL and Si-IL are investigated. The Fe_3O_4-Si-IL and Si-IL nanocomposites show excellent chemical adsorption capacities as 653 and 472 mg g^{-1}, respectively, during times ranging 90 to 110 min when they are used as adsorbents to remove Congo red (CR) dye as a water pollutant.

Keywords: adsorbents; imidazolium cations; ionic liquid; nanocomposite; magnetite; silica nanoparticles

---

1. Introduction

Pure and uncontaminated water is the most important basic requirement of life for all living things on Earth. More than 71% of the Earth's surface is covered with water, but only 1% of water is drinkable as per international standards due to the presence of natural and industrial pollutants. The microorganisms, organic chemicals, and heavy metal pollutants present in water are very dangerous for human health, aquatic systems, and the environment, even in trace amounts [1–3]. There are different methods based on physical, chemical, and biological combinations which are used for water purification. The adsorption of pollutants onto adsorbent surfaces is known to be one of the simplest and most eco-friendly, economically feasible, and effective techniques for industrial wastewater purification [4–6]. There are different types of adsorbents such as natural, biomass, agricultural, and industrial waste adsorbents used as solid adsorbents for wastewater purification [4]. Moreover, advanced adsorbents based on polymers and nanomaterials such as carbon-based nanomaterials (carbon nanotubes and graphene), noble-metal-based nanomaterials, metal oxides (silica, titania, zirconia, and zinc oxides), nanocomposites, magnetic nanocomposites, dendritic polymers, and geopolymer cement have been reported for the desalination and removal of different pollutants from wastewater [5–10]. However, nanomaterials have to face some inherent technical problems when being applied to the production of large-scale adsorbents in water treatments such as aggregations, potentially adverse effects imposed on human health and ecosystems, difficult separation, and leakage into water systems. These problems can be solved by using environmentally friendly magnetic functionalized nanocomposites to emerge

and integrate the merits of functional nanoparticles and vary the solid hosts of the large sizes of materials [8–10]. Although magnetic nanocomposites have achieved excellent results with adsorption and reuse for different cycles in the field of water treatment, some research challenges exist for their application to remove some pollutants such as toxic radioactive metals and organic and agricultural pollutants [9].

The concept of a synergistic combination of two nanoparticles into a larger one has become one of the proposed synthetic techniques used to design advanced nano-adsorbents for water treatments [11–14]. Most of these materials are based on mesoporous silica-based adsorbents [15–17]. The large pore sizes, high specific area, good thermal and chemical stability, low manufacture cost, and excellent selectivity towards specific pollutants elect the ordered mesoporous silica composites as excellent adsorbents for water purification and treatment [17–19]. Highly dispersed and magnetic silica nanoparticles with large-scale chemical or sonochemical synthesis methods have been reported [20–25]. With the large amount of literature available for the production of magnetic silica nanoparticles and with research still being published, perhaps some of the biggest challenges to overcome regard the production of greener selective magnetic silica nano-adsorbents for removal of organic pollutants; these are still a problem facing researchers. Organic cationic and anionic salts based on imidazolium, pyridinium, and quaternary ammonium cations which have been designated as ionic liquids (ILs) are widely used as greener extraction solvents for seawater desalination and industrial water and activated sludge treatments [26–29]. Poly (ionic liquid) (PIL) nanoparticles are used as flocculants for water purification [28], and hydrophobic PILs have been used for the selective separation of methylene blue (MB) dye and chromium ions from water [30]. In our previous works [31–33], PILs were used to prepare ordered nanoparticles with high surface charges, thermal and chemical stability, and high dispersion in aqueous systems to remove the pollutants from the water. This work aims to prepare for the first time novel porous magnetic silica nanocomposites by using aminopropyltriethoxysilane (APTS) as a reagent to prepare imidazolium ILs followed by hydrolysis and linking with magnetite in a basic medium. Moreover, the application and characterization of the produced magnetic silica-ILs as a greener, porous, and selective nanocomposite used to quickly remove MB from wastewater for different cycles are further goals of the present work.

2. Experimental Section

2.1. Materials

All chemicals used in this work were obtained from Sigma-Aldrich Chemicals Co. (Missouri, MO, USA) and used without further purification. The reagents used to prepare the silica-ionic liquids were APTS, glyoxal monohydrate (GA), acetic acid, and *p*-hydoxybenzaldehyde (PHB). The reagents used to prepare magnetite were ferric chloride hexahydrate ($FeCl_3 \cdot 6H_2O$), potassium iodide (KI), and ammonium hydroxide (25%). Congo red (CR) was purchased and utilized to prepare stock solutions of 50–300 mg L^{-1}. A phosphate buffer solution (H_3PO_4/NaH_2PO_4) was used to adjust the pH of aqueous solutions ranging 7–12, while acetate buffer adjusted the pH in the range 3.6–5.6.

2.2. Preparation Techniques

APTS (0.1 mol, 18.5 g) was mixed with 50 mL of acetic acid aqueous solution (50 vol%) in an ice bath at −4 °C. GA (0.02 mol, 1.52 g) was mixed with PHB (0.02 mol, 2.4 g) in 50 mL of acetic acid aqueous solution (50 vol%) at −4 °C to prepare the aldehyde solution. The APTS solution was added to the aldehyde solution under vigorous stirring and heated at 70 °C for 5 h. The reaction mixture was washed several times with diethyl ether to obtain a colorless organic phase. The reaction product was obtained after solvent evaporation using a rotary evaporator. The yield percentage of the reaction was 95% and the product disiloxyimidazolium ionic liquid was designated as SIMIL. Magnetite nanoparticles were synthesized via the reacting of ferric chloride with potassium iodide in the presence of alkaline solution [32]. Briefly, a solution of anhydrous $FeCl_3$ (4 g, dissolved in 30 mL)

was mixed and stirred with KI (1.32 g, dissolved in distilled water (5 mL)) at room temperature under an N_2 atmosphere for one hour to keep the mixture oxygen-free. The iodine byproduct was removed by filtration of the reaction mixture. The filtrate was heated to 40 °C under vigorous stirring, and then ammonia solution (25%, 20 mL) was added dropwise to the filtrate with stirring for another 30 min at 50 °C. The Fe_3O_4 nanoparticles were separated from the mixture by an external magnet and washed with a water–ethanol mixture three times and then dried under vacuum. SIMIL (1 g) was dissolved into a 35% ammonia solution/ethanol mixture (100 mL, 50/50). Magnetite (1 g) was dispersed in the SIMIL solution by sonication for 5 min. Then, the reaction mixture was heated to 35 °C and stirred for 36 h until the complete hydrolysis of silicate occurred to form a magnetic silica IL (Fe_3O_4-Si-IL) that collected using an external magnet and was washed several times using a water:ethanol mixture (50:50). The Fe_3O_4-Si-IL yield percentage of the reaction was 98.9%. The Si-IL was prepared under the same conditions in the absence of magnetite with the reaction yield percentage being 97.6%.

2.3. Characterization of the Prepared Composites

The chemical structures of the prepared silicate and SIMIL, Fe_3O_4-Si-IL, and Si-IL composites were elucidated using Fourier transform infrared analysis (Nicolet Magna 750 FTIR spectrometer using KBr, Newport, NJ, USA) and hydrogen nuclear magnetic resonance (^{1}HNMR) spectroscopy recorded on a 400 MHz 400 MHz Bruker Avance DRX-400 spectrometer (Toronto, ON, Canada). Their thermal stability was determined using thermogravimetric analysis (TGA; NETZSCH STA 449 C instrument, New Castle, DE, USA) under an N_2 atmosphere with heating rate 10 °C min^{-1}. X-ray powder diffraction (X'Pert, Philips, Amsterdam, Netherlands, using CuKa radiation of wavelength λ = 1.5406 °A) was utilized to identify the crystal lattice structures and diffraction patterns of the Fe_3O_4-Si-IL and Si-IL. The particle size, polydispersity index (PDI), and zeta potential of Fe_3O_4-Si-IL and Si-IL were determined using dynamic light scattering (DLS) (Malvern Instrument Ltd., London, UK) at different pHs. The surface morphologies of Fe_3O_4, Fe_3O_4-Si-IL, and Si-IL were studied by transmission electron microscopy (TEM JEOL JEM-2100 F at acceleration voltage of 200 kV, JEOL, Tokyo, Japan) and scanning electron microscopy (JEOL JXA-840A) at 200 kV. The magnetic properties of the Fe_3O_4 and Fe_3O_4-Si-IL were measured using a vibrating sample magnetometer (VSM; USALDJ9600-1; LDJ Electronics, Troy, MI, USA) at room temperature. Brunauer-Emmett-Teller (BET) was used to determine the surface area, the pore volume, and the pore-size distribution of Fe_3O_4-Si-IL and Si-IL powders by the nitrogen adsorption–desorption process using the adsorption data in the relative pressure (P/P_0) range of 0.05–0.3 using a Belsorp-mini II (BEL; Tokyo, Japan).

2.4. CR Adsorption

A UV−visible spectrophotometer (Shimadzu UV-1208 model; Canby, OR, USA) was used to determine the adsorption characteristics of Fe_3O_4-Si-IL and Si-IL adsorbents to remove CR from water. A UV–visible spectrophotometer was used to determine the CR absorbance at wavelengths of 496, 495, and 564 nm at pHs of 9, 7, and 4, respectively. The adsorption capacities of CR dye at equilibrium qe (mg g^{-1}) and the adsorption efficiency E (%) were determined using $qe = (Co - Ce) \times V/m$ and E (%) = $(Co - Ce) \times 100/Co$, where Co, Ce, V and m are the dye concentration in aqueous solutions at time zero at equilibrium (mg L^{-1}), the volume of the aqueous solution (L), and the adsorbent mass (g), respectively. The optimum conditions such as effective Fe_3O_4-Si-IL and Si-IL adsorbent weights, the pH of aqueous solutions, and contact times on the CR maximum adsorption capacity were determined at constant room temperature, and ionic strength 0.01 M and a CR of 100 mg g^{-1}. The optimum conditions of pH, contact time, and weight of Fe_3O_4-Si-IL and Si-IL adsorbents are used to study their adsorption isotherms and kinetics to remove CR from the aqueous solution and to purpose the predominant adsorption removal mechanism. Temperatures of aqueous solutions ranging 298 to 313 K were used to investigate thermodynamic parameters such as standard Gibbs energy (ΔG_o; in kJ mol^{-1}), enthalpy (ΔH_o; in kJ mol^{-1}), and entropy (ΔS_o; in J mol^{-1} K) of the CR adsorption on the Fe_3O_4-Si-IL and Si-IL adsorbent surfaces.

The CR was desorbed from CR-loaded SI-IL and Fe$_3$O$_4$-Si-IL by washing with water and stirring in 25 mL of water followed by stirring in 25 mL of 0.1 M of NaOH solution for 3 h. The concentration of CR was determined as reported in the adsorption section and the desorption efficiency (DE%) of CR was calculated as the ratio of the desorption capacity (q_{de}) and adsorption capacity (q_e). The reusability of the regenerated SI-IL and Fe$_3$O$_4$-Si-IL was checked using seven cycles of consecutive adsorption–desorption studies.

3. Results and Discussion

The present work aimed to prepare novel hybrid silica nanoparticles linked with imidazolium ILs to control their sizes, shapes, surface charges, and thermal and chemical stability. In a previous report imidazolium ILs were prepared by condensation of alkyl amines with GA and PHB under acetic acid conditions [32]. In this respect, APTS was selected as a silane precursor to condense with PHB and GA under acetic acid conditions to produce SIMIL as represented in Scheme 1. The triethoxysilane group at the terminal of SIMIL can hydrolyze with tetraethoxysilane (TEOS) or TEOS and magnetite in the presence of ammonia to produce an Si-IL and Fe$_3$O$_4$-Si-IL hybrid. Ammonia was selected to hydrolyze SIMIL due to it increasing its solubility as an aprotic IL under alkaline conditions more than acidic conditions [34]. The presence of hydroxyl groups on the surface of magnetite [32] facilitates its linking with silica colloids during the hydrolysis of SIMIL under basic conditions.
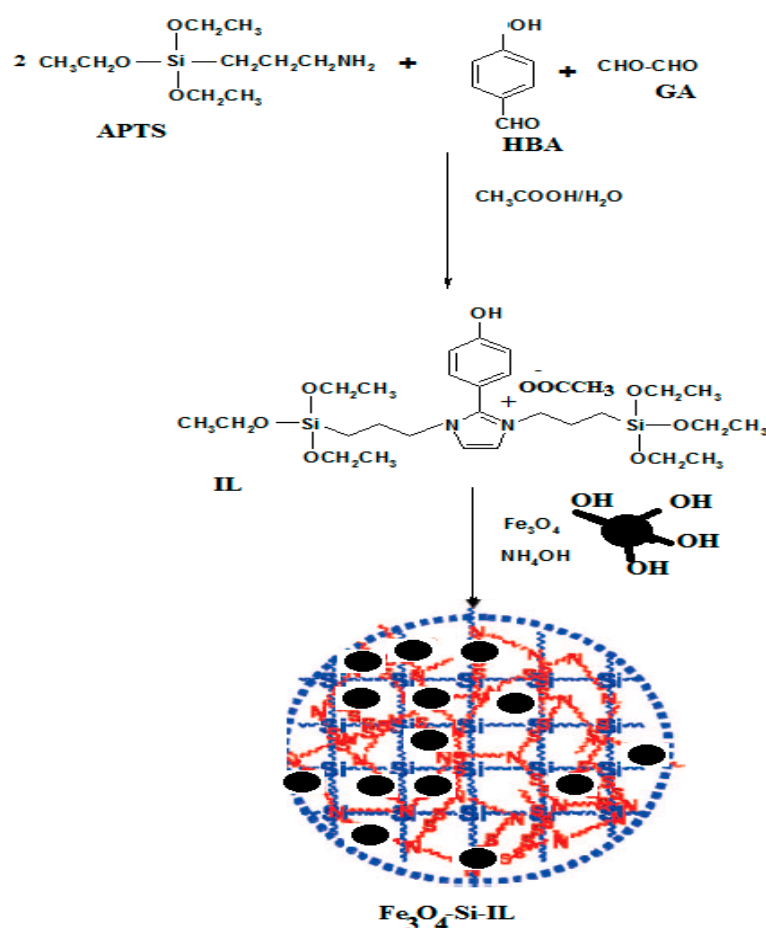
Scheme 1. Synthesis of Fe$_3$O$_4$-Si-IL and Si-IL. *p*-hydroxybenzaldehyde (HBA); APTS, aminopropyltriethoxysilane; GA, glyoxal monohydrate; IL, ionic liquid.

3.1. Characterization

The chemical structure of SIMIL was investigated using the ^{1}HNMR spectrum represented in Figure 1. The formation of imidazolium cations is elucidated by the appearance of a singlet peak at 6.8 ppm related two hydrogen olefin protons. The disappearance of the aldehyde protons of *p*-hydroxybenzaldehyde (HBA) at 9.3 ppm and appearance of peaks at 7.6, 7.3, and 2.3 ppm attributed to four protons of *p*-substituted phenyl rings and phenolic –OH, respectively, confirm the presence of phenol in the chemical structure of SIMIL. The appearance of peaks at 4.19 (m, 2H, CH_2-N^+), 3.64 (m, 2H, CH_2-N), 3.00 (m, 12H, $(CH_2-O)_3$) 1.89 (m, 8H, $2(CH_2)_2$), 1.62 (s, 3H, CH_3COO^-), and 0.55 ppm (m, 18H, $2(CH_3)_3$) elucidate the incorporation of APTS within the chemical structure of SIMIL (Figure 1).
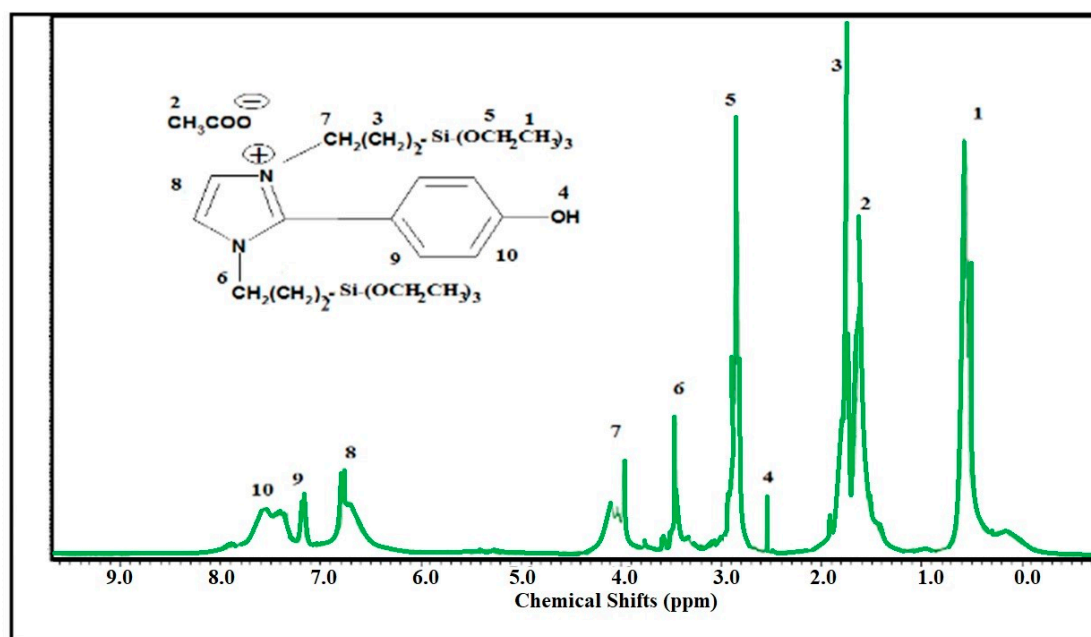

Figure 1. Hydrogen nuclear magnetic resonance (^{1}HNMR) spectrum of disiloxyimidazolium ionic liquid (SIMIL).

The FT-IR spectra of Si-IL and the Fe_3O_4-Si-IL hybrid represented in Figure 2a,b were used to confirm the formation of a silica colloid and the Si-Fe_3O_4 hybrid and to detect their surface structure. There are three bands able to be observed at 580, 1560, and 3607 cm^{-1} in the spectrum of Fe_3O_4-Si-IL (Figure 2b) which correspond to the Fe-O vibration, C=NH stretching of imidazole, and O-H stretching vibration, respectively. The formation of Si-O-Si can be confirmed from the formation of broad bands at 1055–1070 cm^{-1} and 793–938 cm^{-1} which can be attributed to its asymmetric and symmetric stretching vibration, as observed in the spectra of Si-IL and Fe_3O_4-Si-IL (Figure 2a,b). It was noticed that the intensity of the O-H stretching vibration increased after hydrolysis of SIMIL to form colloid Si-IL, which indicated an increase in the content of Si-OH concentration. Moreover, the intensity of the O-H band at 3400 cm^{-1} can be seen to have been reduced in the spectrum of Fe_3O_4-Si-IL, confirming the linking of the hydroxyl groups surrounded on the magnetite surfaces with the hydroxyl groups of Si-OH during the hydrolysis of SIMIL in the presence of magnetite nanoparticles (NPs). These results confirm that the magnetite NPs were coated with silica via the hydrolyzing of TEOS with SIMIL.
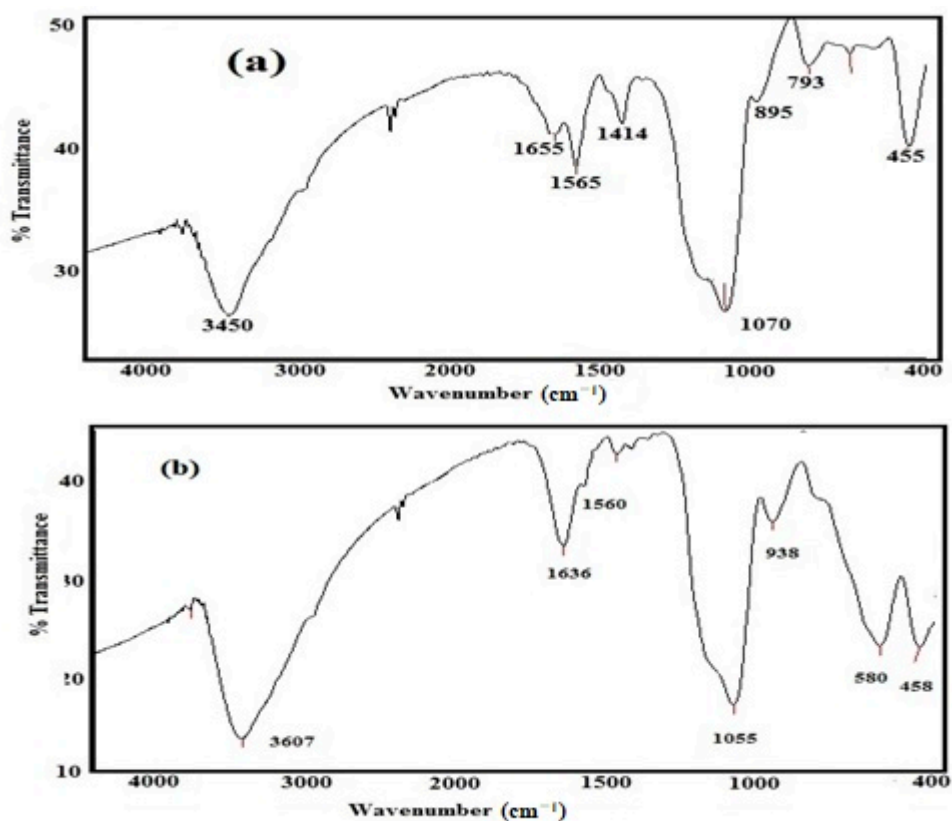
Figure 2. FT-IR spectra of (**a**) Si-IL and (**b**) Fe_3O_4-Si-IL.

The thermal stability and silica or magnetite contents of SIMIL, Si-IL, Fe_3O_4 NPs, and Fe_3O_4-Si-IL hybrid were evaluated using TGA, as represented in Figure 3. The data show that SIMIL was degraded at 325 °C and that the incorporation of magnetite and the formation of silica increased the lost weight (%) by up to 8 wt.% at a temperature starting from 90 °C. This wt.% can be attributed to the humidity and the presence of water contaminated with magnetite, silica colloid and imidazolium ILs [35]. Accordingly, the starting degradation temperatures for Si-IL and Fe_3O_4-Si-IL, determined as the temperature at which the NPs lost approximately 10 wt.%, were 300 and 425 °C, respectively. The strong interaction and linking of magnetite with silica in the Fe_3O_4-Si-IL hybrid improved its thermal stability due to its reducing the plasticization effect of IL [27]. The residual contents of SIMIL, Si-IL, and the Fe_3O_4-Si-IL hybrid after decomposition above 750 °C, determined from their thermograms (Figure 2), can be seen to be 16, 57, and 76 wt.%, respectively. These data determined the pure silica and magnetite contents to be 41 and 18 wt.%, respectively, after subtracting the water and IL contents.
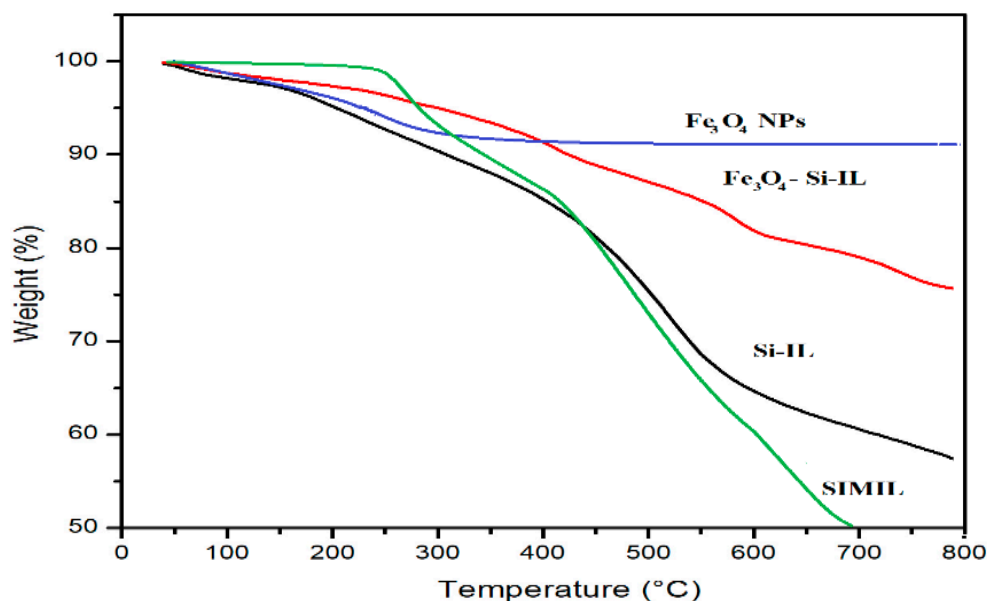
Figure 3. Thermogravimetric analysis (TGA) thermograms of the prepared composites.

The particle size distributions and surface charges of Si-IL and the Fe_3O_4-Si-IL hybrid were evaluated using DLS measurements and have been summarized in Figure 4a–c. The relationship between the surface charges of Si-IL and the Fe_3O_4-Si-IL hybrid and the pH of their aqueous dispersion has been represented in Figure 5 and was used determine their pHs at the isoelectric point (zero surface charges). PDI data confirm the formation of uniform particle sizes when the values decreased below 0.7 and that the particles were more uniform when the values were close to 0.1 [36]. The data of particle sizes of Si-IL (Figure 4a–c) indicate that the hydrolysis of TEOS with SIMIL in basic medium produced silica nanoparticles with sizes ranging from 10.5 to 22.5 nm without the formation of aggregates in aqueous solutions which had different pHs. The presence of Fe_3O_4 during the hydrolysis of TEOS with SIMIL in basic medium produced a Fe_3O_4-Si-IL hybrid with the formation of small aggregates at 5.8 nm via increasing the particle sizes of the silica nanoparticles in the absence of Fe_3O_4 from 10.9 (Si-IL) to 29.6 nm in the presence of Fe_3O_4 (Fe_3O_4-Si-IL). The presence of small particle sizes at 5.8 nm may refer to the presence of free magnetite nanoparticles that non-linked with silica during the hydrolysis. The improvement of dispersity of Fe_3O_4-Si-IL with reduction of PDI values and increasing pH (Figure 4a–c) may be attributed to an increase in their surface charges from +10.9 to −29.7 mV (Figure 5) and repulsive forces between nanoparticles. The negative surface charges of both Si-IL and the Fe_3O_4-Si-IL hybrid indicate the presence of hydroxyl groups at the surface of the silica nanoparticles [37]. Moreover, the positive surface charges of both Si-IL and Fe_3O_4-Si-IL in acidic medium can be attributed to the positive charges of the imidazolium cations. Consequently, it can be concluded that the imidazolium cations oriented as a shell at the surface of Si-IL and the Fe_3O_4-Si-IL hybrid in acidic medium and that their hydroxyl groups oriented as a shell in the basic medium. It can also be noted that the isoelectric points of Si-IL and the Fe_3O_4-Si-IL hybrid were obtained at pH values of 4.8 and 6.6, respectively (Figure 5). This means that the linking of the hydroxyl group of magnetite during the hydrolysis of silica facilitates the orientation of imidazolium cations into the core and their hydroxyl groups as a shell, even in a slightly acidic and neutral aqueous solution. The zeta potential of Fe_3O_4-Si-IL (Figure 5) was less negative when the pH of the aqueous solution increased from 7 to 12 to elucidate the repulsive forces occurring between the magnetite nanoparticles and negative charges of the basic medium besides reducing the interaction of the imidazolium cations of Fe_3O_4-Si-IL with the basic medium. This speculation can be elucidated also when observing the increase in particle sizes of Si-IL from 12.5 to 22.5 nm, as the pH changed from 7 to 9 (Figure 4b,c), when compared to the slight increasing of Fe_3O_4-Si-IL particle sizes from 24.4 to 33.82 nm. The greater increasing of Si-IL compared

to Fe₃O₄-Si-IL particle sizes was able to confirm the higher interaction of imidazolium cations of Si-IL particles with alkaline solution when compared with Fe₃O₄-Si-IL.
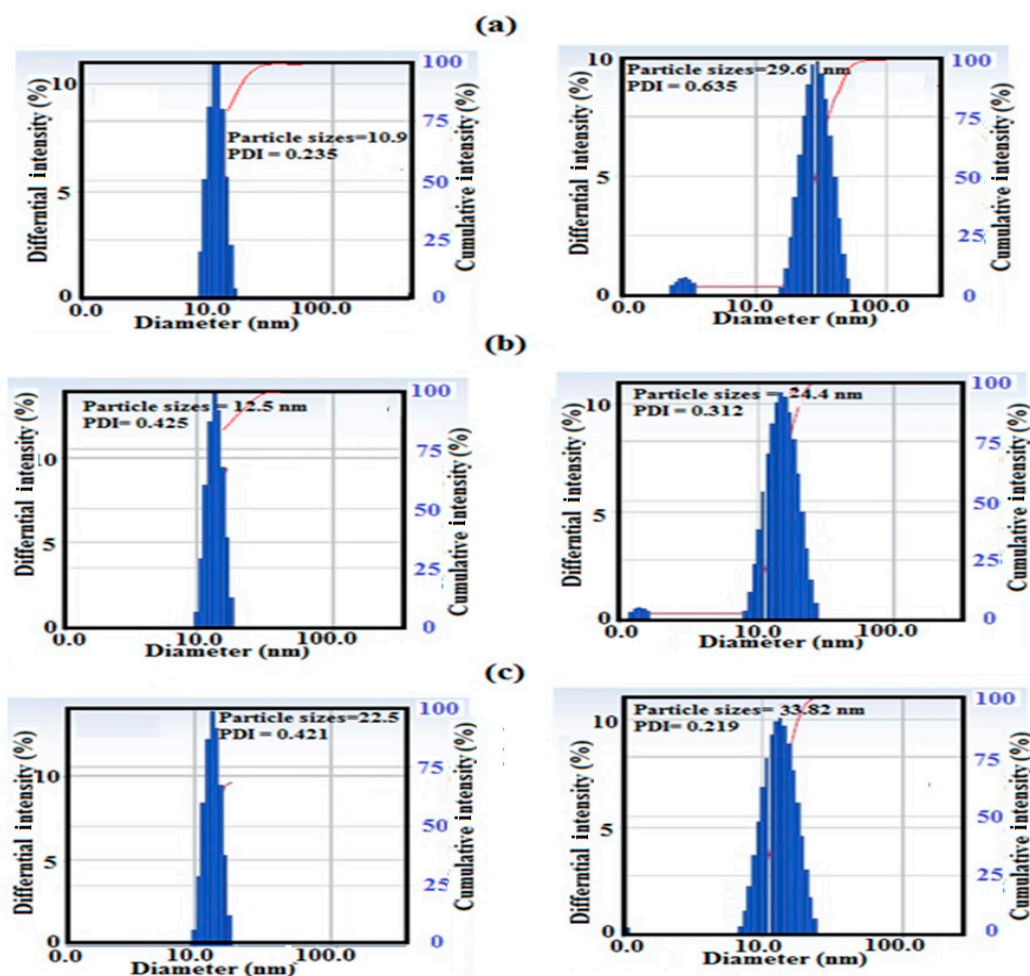

Figure 4. Dynamic light scattering (DLS) data of Si-IL (left) and Fe₃O₄-Si-IL (right) at different pHs, namely, (**a**) 4, (**b**) 7, and (**c**) 9 in aqueous solution in the presence of 0.001 M KCl.
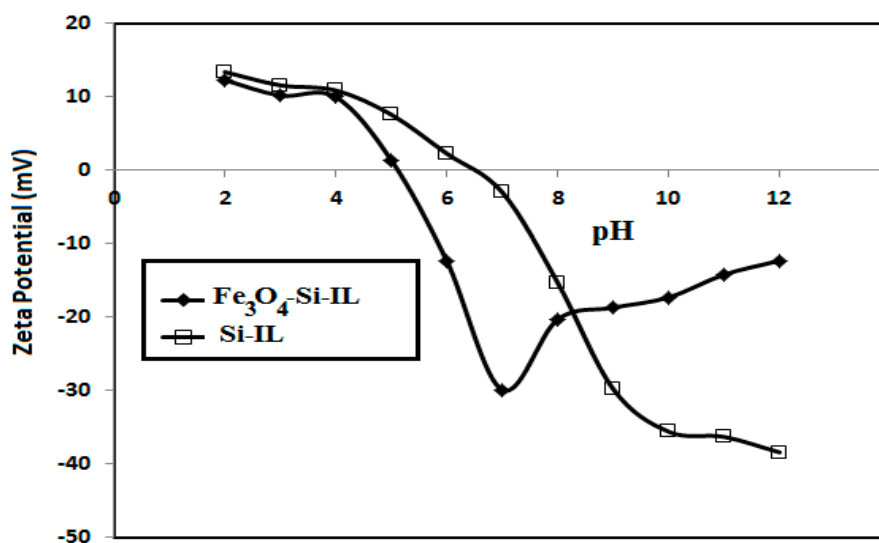

Figure 5. Relationship between zeta potential (mV) and pH of aqueous solution dispersions of Fe₃O₄-Si-IL and Si-IL.

The morphologies of Fe_3O_4, Si-IL, and the Fe_3O_4-Si-IL hybrid were able to be evaluated by high resolution transmittance electron microscope (HR-TEM) micrographs, which are represented in Figure 6a–c, respectively. The data show that spherical nanoparticles were formed in the cases of Si-IL and the Fe_3O_4-Si-IL hybrid (Figure 6b,c). It can also be observed that a porous silica shell was formed in both Si-IL and the Fe_3O_4-Si-IL hybrid (top of Figure 6b,c) on imidazolium IL and magnetite, respectively, as a core. The hydrolysis of SIMIL with TEOS in the presence of ammonia converted the phenol groups of SIMIL to its phenoxy ammoniate ion, increasing the solubility of TEOS and increasing the rate of hydrolysis of SIMIL with TEOS. Consequently, the uniform silica shell increased the repulsive forces among particles to produce highly dispersed uniform Si-IL (Figure 6b). The presence of rhombic magnetite nanoparticles (Figure 6a) changed the polarity of the Fe_3O_4-Si-IL particles to control the interactions of the particles and the thickness of the core-shell morphologies [38].
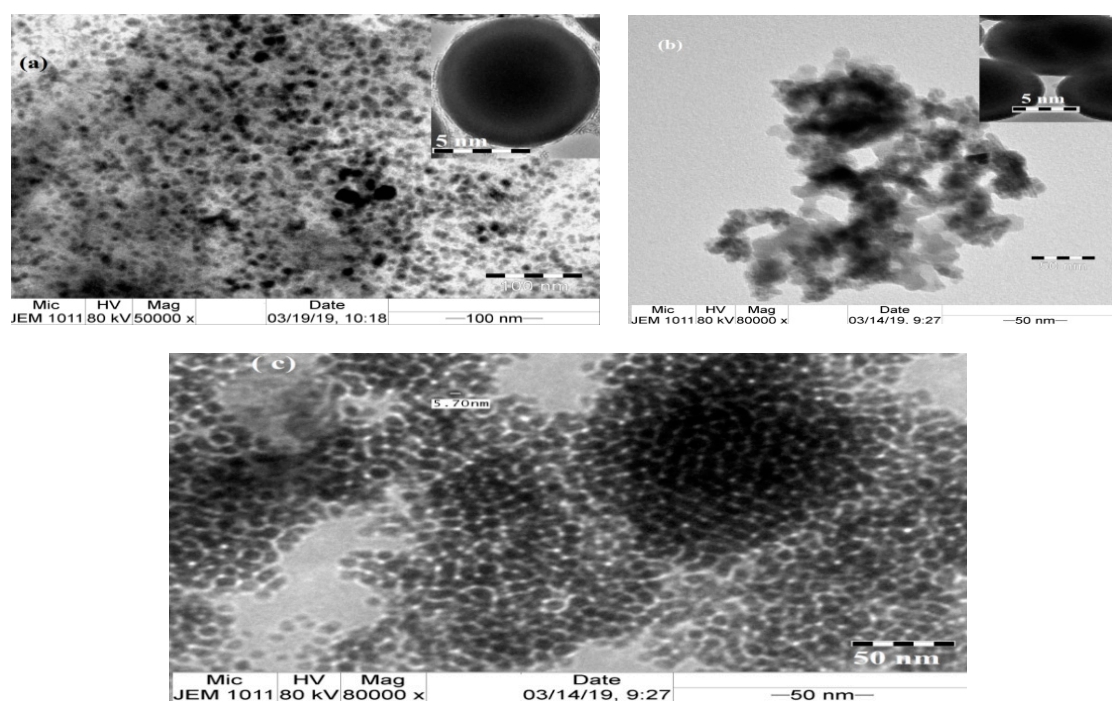

Figure 6. TEM micrographs of (**a**) Si-IL, (**b**) Fe_3O_4-Si-IL, and (**c**) Fe_3O_4.

The lattice structures of Si-IL and the Fe_3O_4-Si-IL hybrid were investigated using their XRD diffractograms, as represented in Figure 7a,b, respectively. The Fe_3O_4-Si-IL hybrid diffractogram indicates that the corresponding peaks and lattice structure magnetite (Figure 7b) used during the hydrolysis of SIMIL with TEOS was pure without oxidation to other iron oxide impurities such as maghemite or hematite [39]. The presence of a broad peak at 2-theta 15–22° confirms the formation of amorphous porous silica shells in both Si-IL and Fe_3O_4-Si-IL, while the multiple high angle peaks relate to the magnetite core of Fe_3O_4-Si-IL (Figure 7a,b).
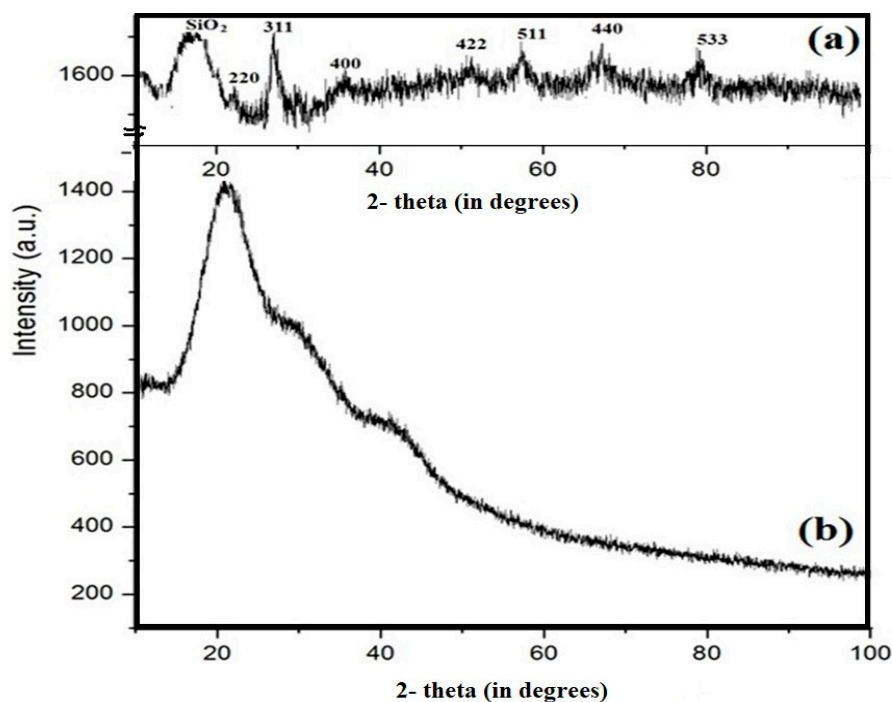
Figure 7. XRD diffractograms of (**a**) Fe_3O_4-Si-IL and (**b**) Si-IL.

The magnetic properties of the Fe_3O_4-Si-IL hybrid were determined using a VSM hysteresis loop (Figure 8). The magnetic properties of Fe_3O_4-Si-IL, including saturation magnetization (Ms; this represents the magnetization of the material at a higher applied value of an external magnetic field H), coercivity (Hc; this measures the reverse field required to reach the magnetization to zero after saturation), and remnant magnetization (Mr; this evaluates the remaining magnetization after removal of the external magnetic field), were found to be 35.3 emu/g, 20.71 G, and 0.38 emu/g, respectively. The Ms, Hc, and Mr of the prepared magnetite NPs had been determined in a previous work [40] as 78.6 emu/g, 8.55 G, and 0.15 emu/g, respectively. The lower Ms value of Si-IL indicates that the magnetite was encapsulated or coated into Si-IL, which reduced its magnetization. The low Hc value of Fe_3O_4-Si-IL confirms that the prepared material possesses superparamagnetic properties.
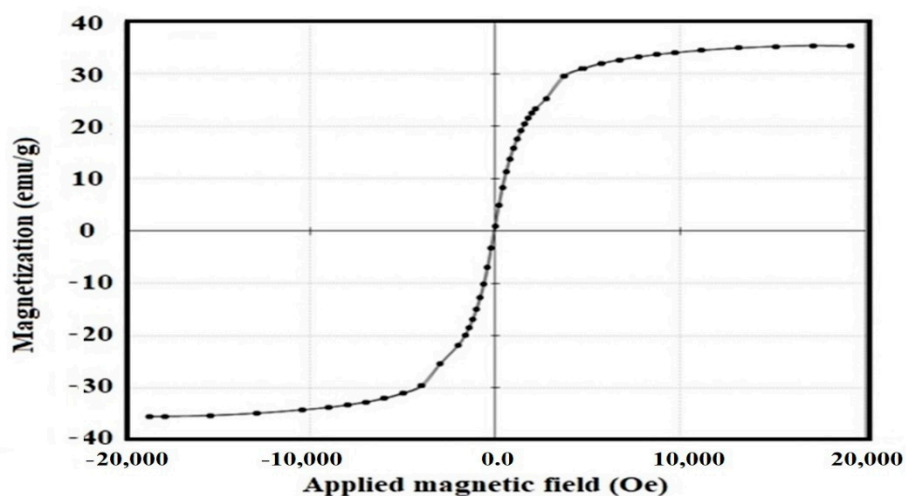

Figure 8. Vibrating sample magnetometer (VSM) hysteresis of the Fe_3O_4-Si-IL hybrid at room temperature.

The pore structure and surface area of Si-IL and Fe_3O_4-Si-IL were estimated from nitrogen adsorption–desorption isotherms at 77 K, which are represented in Figure 9. The samples were pretreated at a temperature of 353 K to remove any water or water humidity from the sample pores [41]. The samples were then heated under vacuum up to 423 K before measuring their surface area and pore sizes. The sorption isotherms of Si-IL and Fe_3O_4-Si-IL (Figure 9) gave rise to type I. The BET surface area (S_{BET}; m^2 g^{-1}), pore sizes (D; nm), and pore volume (V_{total}; cm^3 g^{-1}) of Si-IL were found to be 64, 10.56, and 0.0869, respectively. The D, S_{BET}, and V_{total} values of Fe_3O_4-Si-IL were found to be 92 m^2 g^{-1}, 14.63 nm, and 0.1729 cm^3 g^{-1}, respectively. These data agree with the DLS data (Figure 4a–c) and TEM micrographs (Figure 6b,c) and indicate that the pore sizes increased in the case of Fe_3O_4-Si-IL due to the linking of magnetite with silica to activate the silica surfaces and increase their surface area. These data confirm the formation of the porous structures of Si-IL and Fe_3O_4-Si-IL, which enhance their application as an adsorbent.
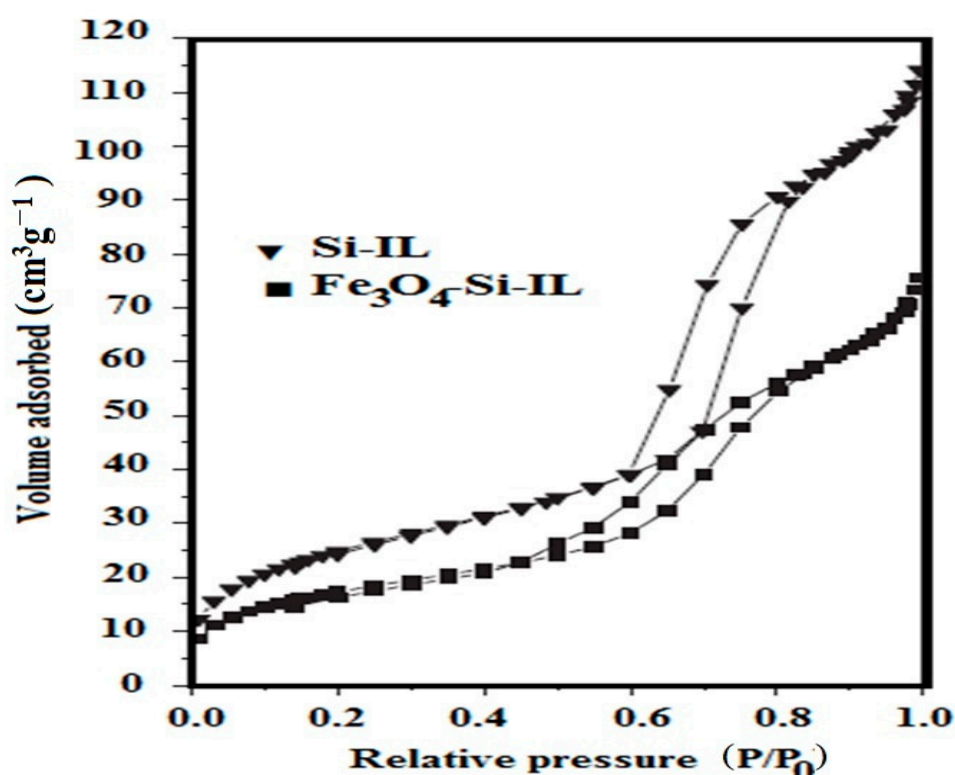

Figure 9. Brunauer-Emmett-Teller (BET) data of the prepared Si-IL and Fe_3O_4-Si-IL.

3.2. Application of Adsorbents for CR Removal

The optimum pHs with which to remove CR from their 20 mL aqueous solution at a concentration of 100 mg L^{-1} were determined from the relationship of removal efficiency ($E\%$) versus pH, which has been plotted in Figure 10, at constant room temperature, ionic strength 0.01 M, and 4 mg of the adsorbents. The optimum pH 4 achieved a higher $E\%$ of both Si-IL and Fe_3O_4-Si-IL of 94.2 and 99.9%, respectively. It may also be noted that $E\%$ decreased dramatically with increasing pH of the aqueous solution to neutral and basic solutions. This observation can be correlated to the reaction of hydroxyl phenolic of SIMIL in the basic medium to produce anionic phenoxide, which was repulsed by the negative charges of CR moieties that increased in the basic or neutral aqueous solution to enhance the electrostatic attraction between the imidazolium site of the adsorbents and the anionic CR dye in the acidic medium [42]. The encapsulation of magnetite inside the shell of Fe_3O_4-Si-IL protects it from leaching or decomposition in acidic solution [43].
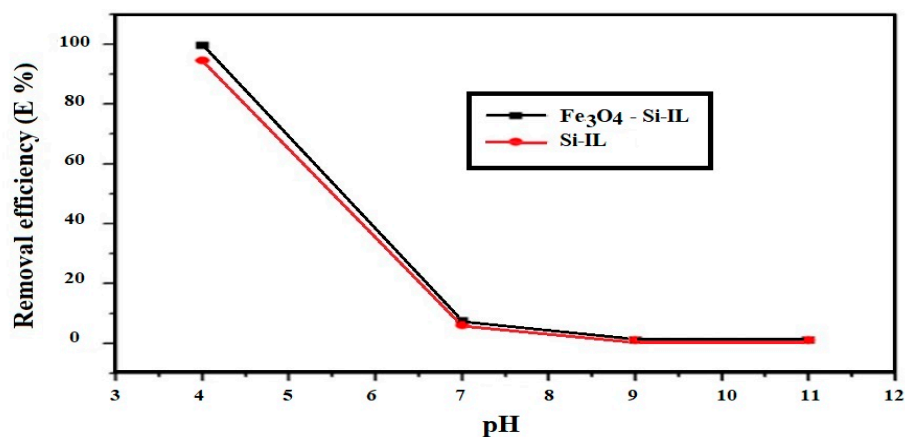
Figure 10. Effect of pH on the removal efficiency (*E*%) of Si-IL and Fe$_3$O$_4$-Si-IL at 0.1 M ionic strength and room temperature.

The optimum weights of the Si-IL and Fe$_3$O$_4$-Si-IL adsorbents to remove 100 mg L^{-1} of CR from 20 mL of aqueous solution at pH 4 and room temperature were determined from the relationship between *E*% or *q* (mg g^{-1}) and adsorbent weights (mg), as represented in Figure 11a,b, respectively. The data show that the optimum weights of the Si-IL and Fe$_3$O$_4$-Si-IL adsorbents which achieved a higher *E*% of CR removal were 3.7 and 3 mg, respectively. Moreover, the *q* and *E*% of the Fe$_3$O$_4$-Si-IL adsorbent (Figure 11b) at its optimum weight were 650 mg g^{-1} and 98.8%, respectively. The Si-IL (Figure 11a) adsorbent displayed a lower *q* and *E*% at its optimum weight, and *q* and *E*% were found to be 476 and 90%, respectively. These data indicate the higher adsorption capacity and removal efficiency at lower optimum weight of Fe$_3$O$_4$-Si-IL compared to Si-IL due to its higher surface area, pore volume, and diameter (BET measurements; Figure 9).
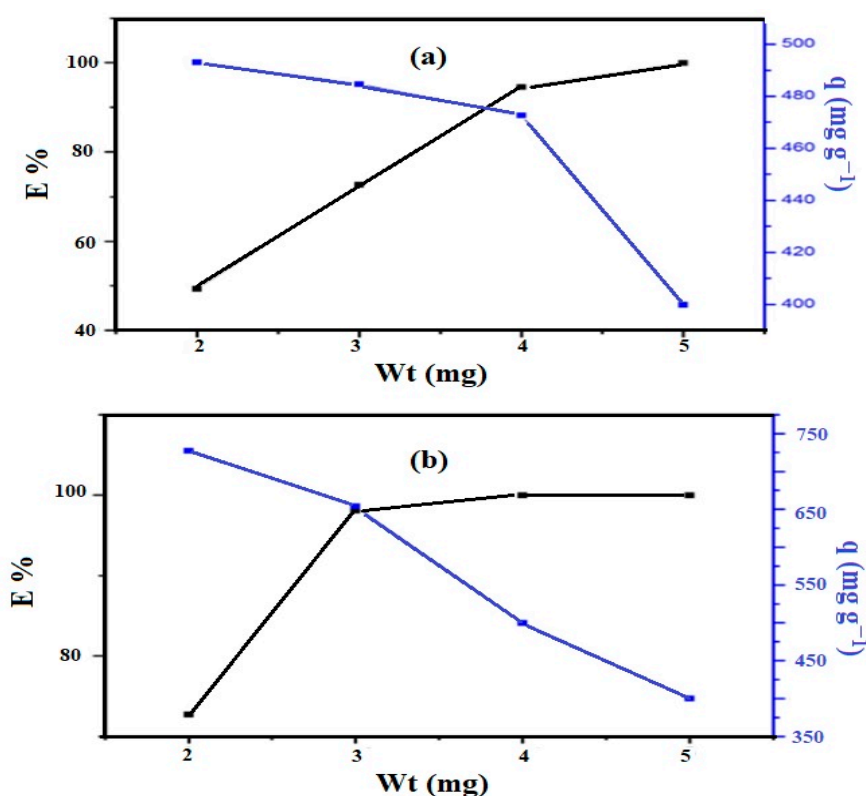

Figure 11. Removal efficiency and adsorption capacity against weight (mg) of (**a**) Si-IL and (**b**) Fe$_3$O$_4$-Si-IL (at constant room temperature using 20 mL of 100 mg L^{-1} of Congo red (CR)).

The effect of contact times on the CR maximum adsorption capacity (q; mg g^{-1}) of both Fe$_3$O$_4$-Si-IL and Si-IL at pH 4 and room temperature and their optimum weights was investigated. The data confirm that Fe$_3$O$_4$-Si-IL and Si-IL achieved maximum q values of 653 and 472 mg g^{-1} at contact times of 110 and 90 min, respectively. Moreover, it may be noted that Fe$_3$O$_4$-Si-IL showed greater q values during all contact times to reach the equilibrium. By comparing our work with previous works aimed at removing CR from aqueous solution [44–47], it was able to be observed that the present system achieved q values ranging 472 to 653 during times ranging 90 to 110 min, which are higher than other systems which achieved q values ranging from 950 to 500 mg g^{-1} during a period of 10 h.

3.3. Adsorption Isotherms

The homogeneity and heterogeneity of the Fe$_3$O$_4$-Si-IL and Si-IL adsorbent surfaces beside the formation of the CR monolayer and multilayers on the adsorbent surfaces were confirmed using the best adsorption isotherms models of Langmuir and Freundlich. The Langmuir and Freundlich adsorption models can be represented using the equations (C_e/q_e) = [($1/Q_{max}K_l$) + (C_e/Q_{max})] and log(q_e) = log(K_f) + [($1/n$) log(C_e)]. The constants n (in g L^{-1}), K_l (in L mg^{-1}), and K_f (in (mg g^{-1})(L mg^{-1})$^{(1/n)}$) are the empirical constant, Langmuir constant, and Freundlich constant, respectively. The adsorption parameters of the Langmuir and Freundlich equations related to the Fe$_3$O$_4$-Si-IL and Si-IL adsorbents are listed in Table 1. The linear relationships of both the Fe$_3$O$_4$-Si-IL and Si-IL adsorbents with the highest linear coefficient (R^2) (Table 1) reveal that the present system obeyed the Langmuir more than the Freundlich adsorption model. This means that both the Fe$_3$O$_4$-Si-IL and Si-IL adsorbents had homogenous surfaces and formed a monolayer of CR adsorbate on their surfaces. Moreover, the good agreement between the theoretical adsorption capacity Q_{max} (mg g^{-1}) and experimental value q_e using the Langmuir model proves that the adsorption process obeyed the Langmuir model.

The essential characteristic of the Langmuir isotherm can be expressed in terms of a dimensionless constant separation factor (RL; also called the equilibrium parameter) which is given by the equation $RL = 1/(1 + KlCo)$, where Co (mg/L) is the highest initial CR dye concentration (mg L^{-1}) [48]. The *RL* values of the Fe$_3$O$_4$-Si-IL and Si-IL adsorbents were found to be 0.009855 and 0.009853, respectively, which indicates that the adsorption of CR on their surfaces was favorable because the $0 < RL < 1$. Additionally, the Fe$_3$O$_4$-Si-IL and Si-IL adsorbents showed lower *RL* values at higher initial CR concentrations, confirming that the adsorption was more favorable at a higher concentration. This degree of favorability is generally related to the irreversibility of the system, giving a qualitative assessment of the interactions of Fe$_3$O$_4$-Si-IL and Si-IL towards CR. The *RL* tended toward zero, confirming the completely ideal irreversible adsorption case of CR on the Fe$_3$O$_4$-Si-IL or Si-IL surfaces rather than unity (which represents a completely reversible case).

Table 1. Adsorption isotherm parameters of CR dye using Fe$_3$O$_4$-Si-IL and Si-IL composites at 298 K and optimum adsorption parameters.

Adsorbents	Langmuir Isotherm Parameters			Freundlich Isotherm Parameters			q_e
	Q_{max} mg g^{-1}	K_l L mg^{-1}	R^2	n g L^{-1}	K_f ((mg g^{-1}) (L mg$^{-1(1/n)}$))	R^2	Mg g^{-1}
Fe$_3$O$_4$-Si-IL	709.09	0.458333	0.998	5.29	398.1072	0.58	653
Si-IL	476.19	0.488372	0.993	8.77	275.4229	0.46	472

3.4. Adsorption Kinetics

The adsorption rates of Fe$_3$O$_4$-Si-IL and Si-IL adsorbents to remove CR from aqueous solutions were able to be estimated and analyzed using pseudo first-order and pseudo second-order models [49] and have been tabulated in Table 2. The higher correlation coefficient (R^2) and the agreement of the calculated $q_{e,cal}$ values of the fitted curves obtained by the pseudo second-order kinetic model with the experimental $q_{e,exp}$ values prove that the pseudo second-order model is the predominant means

by which to describe the adsorption process. These data mean that the adsorption capacities of the Fe_3O_4-Si-IL and Si-IL adsorbents are more dependent on the CR concentrations. By comparing the adsorption rate constant (K_2; Table 2) of the present system with other IL systems reported in the literature [44–47], it was able to be found that the present systems for both the Fe_3O_4-Si-IL and Si-IL adsorbents have a higher and faster rate of removal of CR as compared to other PILs. Moreover, the removal rate of Fe_3O_4-Si-IL was found to be two times faster than Si-IL (K_2; Table 2). This means the adsorption capacity was more dependent on the surface adsorbate amount [4].

Table 2. Kinetic parameters of Fe_3O_4-Si-IL and Si-IL composites for removal of CR from aqueous solution at 298 K.

Adsorbents	q_{exp} (mg g^{-1})	Pseudo Second-Order				Pseudo First-Order		
		Kinetic Parameters				Kinetic Parameters		
		$q_{calc.}$ (mg g^{-1})	$K_2 \times 10^4$ (g mg^{-1} min^{-1})	R^2		$q_{calc.}$ (mg g^{-1})	K_1 (min^{-1}) 10^{-2}	R^2
Fe_3O_4-Si-IL	653	714.28	1.041	0.998		415.91	0.028788	0.97
Si-IL	472	588.23	0.622	0.994		404.66	0.026024	0.95

The effect of temperature on thermodynamic parameters such as standard Gibbs energy (ΔG_o; in kJ mol^{-1}), enthalpy (ΔH_o; in kJ mol^{-1}), and entropy (ΔS_o; in J mol^{-1} K) of CR adsorption on the Fe_3O_4-Si-IL and Si-IL adsorbent surfaces were investigated and calculated using the equations $\Delta G_o = -RT \ln(C_eA/C_e)$ and $\log(C_eA/C_e) = \Delta S_o/2.303R - \Delta H_o/2.303RT$, where C_eA, R, and T are the adsorbent concentration (in mg L^{-1}), gas constant (8.314 J mol^{-1} K^{-1}), and the aqueous solution temperature (in K), respectively. The values of ΔG_o, ΔH_o, and ΔS_o of Fe_3O_4-Si-IL and Si-IL have been given in Table 3. The equilibrium concentration constant (K_c) was able to be calculated from the relation (C_eA/C_e) for Fe_3O_4-Si-IL and Si-IL and has been plotted in Figure 12. It may be noted from the data in Table 3 that the higher negative value of ΔG_o for Fe_3O_4-Si-IL compared to Si-IL with increasing temperature highlights the spontaneous nature of the CR dye adsorbed on the Fe_3O_4-Si-IL adsorbent at a higher rate than Si-IL. The positive values of ΔH_o and ΔS confirm that the adsorption of the CR adsorbate on the Fe_3O_4-Si-IL and Si-IL surfaces was endothermic, and also indicates an increase in the degrees of freedom of the CR species on the surface of the adsorbent with increasing temperature [50]. Moreover, these values show that an increase in the concentration of the CR dye molecules at the solid–liquid interface increased its adsorption onto the Fe_3O_4-Si-IL and Si-IL surfaces.

Table 3. Thermodynamic parameters of Fe_3O_4-Si-IL and Si-IL for removal of CR from aqueous solution at different temperatures.

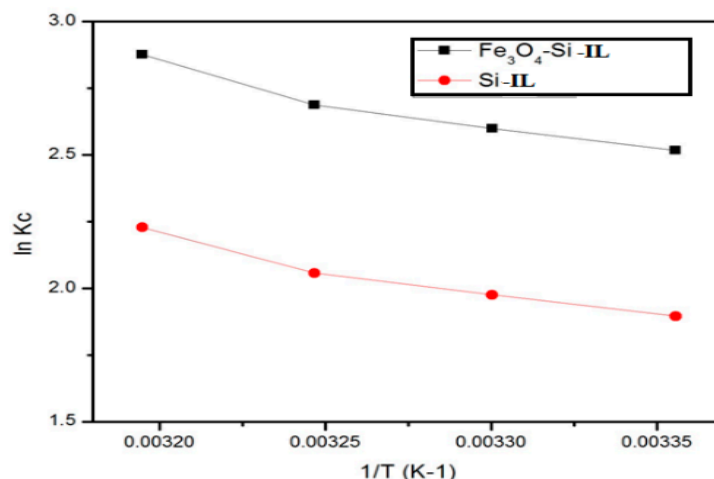| Adsorbents	ΔH^0 (kJ mol^{-1})	ΔS^0 (J mol^{-1})	ΔG^0 (kJ mol^{-1})			
			298 K	303 K	308 K	313 K
Fe_3O_4-Si-IL	18.10	81.31	−6.131	−6.537	−6.944	−7.35
Si-IL	16.71	71.66	−4.646	−5.011	−5.363	−5.721

Figure 12. Plot of $\ln K_c$ (the equilibrium concentration constant) versus $1/T$ for Si-IL and Fe_3O_4-Si-IL at the temperature range of 303–333 K.

The previous data were used to confirm the proposed adsorption mechanism represented in Scheme 2 for removal of CR from the aqueous solution by using Fe_3O_4-Si-IL and Si-IL adsorbents. In this respect, the porous, uniform, and ordered surfaces of Fe_3O_4-Si-IL and Si-IL can be seen to have facilitated the formation of a monolayer of CR on their surfaces, as elucidated from the Langmuir isotherm (Table 1). The CR diffused into the porous structure of Fe_3O_4-Si-IL and Si-IL, which was confirmed via TEM (Figure 6), BET measurements (Figure 9), and the fact that the adsorption capacity increased by ion exchange with the chemical binding. Moreover, SIMIL is shown to play a significant role in increasing the CR adsorption capacity. It is responsible for the formation of a strong hydrogen bond, ion exchange CR anions, and CH_3COO^- counter-ions, and the electrostatic interaction between the imidazolium cations of the adsorbent and the sulfonate anion of the adsorbate are responsible for the chemisorption nature of Fe_3O_4-Si-IL and Si-IL toward CR dye [51,52].
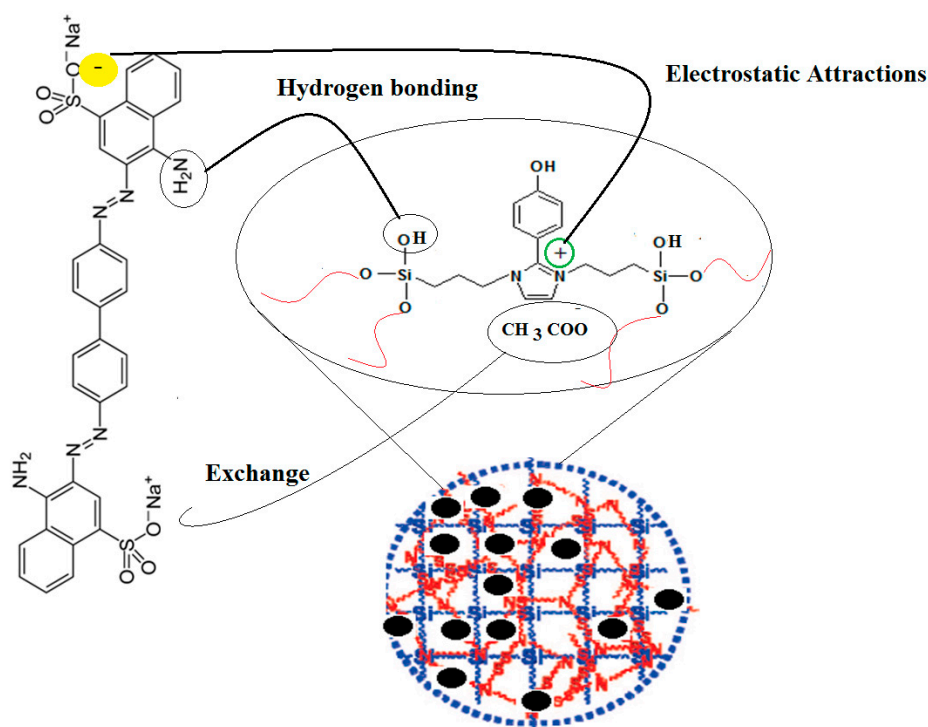
Scheme 2. Chemical adsorption of CR on Fe_3O_4-Si-IL and Si-IL surfaces.

A comparison between the adsorption efficiencies of the Fe_3O_4-Si-IL and Si-IL nanocomposites and other sorbents was carried out, as displayed in Table 4. The prepared nanocomposites removed CR dye from water with higher capacities and in shorter times compared to other adsorbents [53–55]. The porous structures of Si-IL and Fe_3O_4-Si-IL enabled them to adsorb CR dye with a high capacity. In addition, the imidazolium cation in the silicate network facilitated the CR adsorption through an electrostatic interaction mechanism.

Table 4. A comparison of the adsorption performance of different adsorbents.

Adsorbent	Contact Time (min)	Q_{max} (mg/g)	Reference
Activated carbon	1440	105	51
Magnetite nanoparticle	40	68.5	52
Chitosan/organomontmorillonite	480	293	53
Fe_3O_4-Si-IL	653	90	This work
Si-IL	160	110	This work

Seven cycles of the desorption–sorption experiments to reuse of Fe_3O_4-Si-IL and Si-IL were performed in basic solution, as reported in the experimental section. The *DE*% of Fe_3O_4-Si-IL and Si-IL were determined. The data indicate that the desorption of CR was completed in basic medium and could not be desorbed in neutral medium, which confirms that the linking between CR and Fe_3O_4-Si-IL and Si-IL is by an ion exchange strong force [56]. The magnetic properties of Fe_3O_4-Si-IL during seven cycles confirmed the bonding of magnetite with silica and the good protection of SIMIL, which prevents further oxidation or leaching of magnetite. The *DE*% of Si-IL shows that the CR dye desorption efficiencies decreased by 75% after the fifth cycle. This could be referred to as the demolition of the electrostatic attraction between the Si-IL and CR molecules.

4. Conclusions

In this work, a new aprotic disiloxyimidazolium ionic liquid SIMIL was hydrolyzed with TEOS or TEOS and magnetite in the presence of ammonia to produce Si-IL and a Fe_3O_4-Si-IL hybrid. The pure silica and magnetite contents of the Fe_3O_4-Si-IL hybrid were 41 and 18 wt.%, respectively. The presence of Fe_3O_4 during the hydrolysis of TEOS with SIMIL increased the particle sizes of silica nanoparticles from 10.9 (Si-IL) to 29.6 nm (Fe_3O_4-Si-IL). The imidazolium cations oriented as a shell at the surface of Si-IL and the Fe_3O_4-Si-IL hybrid in acidic medium and their hydroxyl groups were oriented as a shell in the basic medium. The isoelectric points of Si-IL and the Fe_3O_4-Si-IL hybrid were obtained at pH 4.8 and 6.6, respectively. This confirms that the linking of the hydroxyl group of magnetite during the hydrolysis of silica facilitated the orientation of imidazolium cations into the core and their hydroxyl groups as a shell, even in slightly acidic and neutral aqueous solution. The uniform silica shell increased the repulsive forces among particles to produce a highly dispersed uniform Si-IL. The presence of rhombic magnetite nanoparticles changed the polarity of the Fe_3O_4-Si-IL particles to control the interactions of the particles and the thickness of the core–shell morphologies. BET data confirmed the formation of the porous structures of Si-IL and Fe_3O_4-Si-IL. The Fe_3O_4-Si-IL and Si-IL nanocomposites showed excellent chemical adsorption capacities of 653 and 472 mg g^{-1}, respectively, during times ranging from 90 to 110 min when they were used as adsorbents to remove CR dye as a water pollutant.

Author Contributions: Conceptualization, methodology, investigation, and writing—review and editing, A.M.A. and A.O.E.; supervision, Y.M.M. and A.I.H.; funding acquisition and data curation, A.M.A. and A.O.E. All authors have read and agreed to the published version of the manuscript.

Conflicts of Interest: The authors declare no conflict of interest.

References

1. Jamil, M.; Zia, M.S.; Qasim, M. Contamination of agro-ecosystem and human health hazards from wastewater used for irrigation. *J. Chem. Soc. Pak.* **2010**, *32*, 370–378.

2. Khan, S.; Cao, Q.; Zheng, Y.; Huang, Y.; Zhu, Y.G. Health risks of heavy metals in contaminated soils and food crops irrigated with wastewater in Beijing, China. *Environ. Pollut.* **2008**, *152*, 686–692. [CrossRef] [PubMed]

3. Peng, S.H.; Wang, W.X.; Li, X.; Yen, Y.F. Metal partitioning in river sediments measured by sequential extraction and biomimetic approaches. *Chemosphere* **2004**, *57*, 839–851. [CrossRef] [PubMed]

4. Atta, A.M.; Ezzat, A.O.; Moustafa, Y.M.; Sabeela, N.I.; Tawfeek, A.M.; Al-Lohedan, H.A.; Hashem, A.I. Synthesis of New Magnetic Crosslinked Poly (Ionic Liquid) Nanocomposites for Fast Congo Red Removal from Industrial Wastewater. *Nanomaterials* **2019**, *9*, 1286. [CrossRef]

5. Rivera, F.L.; Palomares, F.J.; Herrasti, P.; Mazario, E. Improvement in Heavy Metal Removal from Wastewater Using an External Magnetic Inductor. *Nanomaterials* **2019**, *9*, 1508. [CrossRef]

6. Teow, Y.H.; Mohammad, A.W. New generation nanomaterials for water desalination: A review. *Desalination* **2019**, *451*, 2–17. [CrossRef]

7. Zhang, Y.; Wu, B.; Xu, H.; Liu, H.; Wang, M.; He, Y.; Pan, B. Nanomaterials-enabled water and wastewater treatment. *NanoImpact* **2016**, *3*, 22–39. [CrossRef]

8. Mehta, D.; Mazumdar, S.; Singh, S. Magnetic adsorbents for the treatment of water/wastewater—A review. *J. Water Process Eng.* **2015**, *7*, 244–265. [CrossRef]

9. Lingamdinne, L.P.; Koduru, J.R.; Karri, R.R. A comprehensive review of applications of magnetic graphene oxide based nanocomposites for sustainable water purification. *J. Environ. Manag.* **2019**, *231*, 622–634. [CrossRef]

10. Zhao, X.; Lv, L.; Pan, B.; Zhang, W.; Zhang, S.; Zhang, Q. Polymer-supported nanocomposites for environmental application: A review. *Chem. Eng. J.* **2011**, *170*, 381–394. [CrossRef]

11. Kabiri, S.; Tran, D.N.H.; Cole, M.A.; Losic, D. Functionalized three-dimensional (3D) graphene composite for high efficiency removal of mercury. *Environ. Sci. Water Res. Technol.* **2016**, *2*, 390–402. [CrossRef]

12. Qin, Q.; Xu, Y. Enhanced nitrobenzene adsorption in aqueous solution by surface silylated MCM-41. *Microporous Mesoporous Mater.* **2016**, *232*, 143–150. [CrossRef]

13. Cho, S.; Kim, N.; Lee, S.; Lee, H.; Lee, S.H.; Kim, J.; Choi, J.W. Use of hybrid composite particles prepared using alkoxysilane-functionalized amphiphilic polymer precursors for simultaneous removal of various pollutants from water. *Chemosphere* **2016**, *156*, 302–311. [CrossRef] [PubMed]

14. Diagboya, P.N.; Dikio, E.D. Scavenging of aqueous toxic organic and inorganic cations using novel facile magneto-carbon black-clay composite adsorbent. *J. Clean. Prod.* **2018**, *180*, 71–80. [CrossRef]

15. Li, N.; Fu, F.; Lu, J.; Ding, Z.; Tang, B.; Pang, J.; Rodriguez, A.G.P. Facile preparation of magnetic mesoporous $MnFe_2O_4@SiO_2-CTAB$ composites for Cr(VI) adsorption and reduction. *Environ. Pollut.* **2017**, *220*, 1376–1385. [CrossRef]

16. Husnain, S.M.; Kim, J.H.; Lee, C.S.; Chang, Y.Y.; Um, W.; Chang, Y.S. Superparamagnetic nalidixic acid grafted magnetite (Fe_3O_4/NA) for rapid and efficient mercury removal from water. *RSC Adv.* **2016**, *6*, 35825–35832. [CrossRef]

17. Diagboya, P.N.; Olu-Owolabi, B.I.; Adebowale, K.O. Microscale scavenging of pentachlorophenol in water using amine and tripolyphosphate-grafted SBA-15 silica: Batch and modeling studies. *J. Environ. Manag.* **2014**, *146*, 42–49. [CrossRef]

18. Wu, Z.; Zhao, D. Ordered mesoporous materials as adsorbents. *Chem. Commun.* **2011**, *47*, 3332–3338. [CrossRef]

19. Diagboya, P.N.; Dikio, E.D. Silica-based mesoporous materials; emerging designer adsorbents for aqueous pollutants removal and water treatment. *Microporous Mesoporous Mater.* **2018**, *266*, 252–267. [CrossRef]

20. Rho, W.Y.; Kim, H.M.; Kyeong, S.; Kang, Y.L.; Kim, D.H.; Kang, H.; Jeong, C.; Kim, D.E.; Lee, Y.S.; Jun, B.H. Facile synthesis of monodispersed silica-coated magnetic nanoparticles. *J. Ind. Eng. Chem.* **2014**, *20*, 2646–2649. [CrossRef]

21. Wang, S.; Tang, J.; Zhao, H.; Wan, J.; Chen, K. Synthesis of magnetite–silica core–shell nanoparticles via direct silicon oxidation. *J. Colloid Interface Sci.* **2014**, *432*, 43–46. [CrossRef] [PubMed]

22. Sun, Y.; Duan, L.; Guo, Z.; Duanmu, Y.; Ma, M.; Xu, L.; Zhang, Y.; Gu, N. An improved way to prepare superparamagnetic magnetite-silica core-shell nanoparticles for possible biological application. *J. Magn. Magn. Mater.* **2005**, *285*, 65–70. [CrossRef]
23. Sodipo, B.K.; Aziz, A.A. One minute synthesis of amino-silane functionalized superparamagnetic iron oxide nanoparticles by sonochemical method. *Ultrason. Sonochem.* **2018**, *40*, 837–840. [CrossRef] [PubMed]
24. Liu, X.; Ma, Z.; Xing, J.; Liu, H. Preparation and characterization of amino–silane modified superparamagnetic silica nanospheres. *J. Magn. Magn. Mater.* **2004**, *270*, 1–6. [CrossRef]
25. Bini, R.A.; Marques, R.F.C.; Santos, F.J.; Chaker, J.A.; Jafelicci, M. Synthesis and functionalization of magnetite nanoparticles with different amino-functional alkoxysilanes. *J. Magn. Magn. Mater.* **2012**, *324*, 534–539. [CrossRef]
26. Chen, Q.; Ge, Q.; Xu, W.; Pan, W. Functionalized imidazolium ionic liquids promote seawater desalination through forward osmosis. *J. Membr. Sci.* **2019**, *574*, 10–16. [CrossRef]
27. Lee, W.G.; Hwang, J.; Kang, S.W. Control of nanoporous polymer matrix by an ionic liquid and water pressure for applications to water-treatment and separator. *Chem. Eng. J.* **2016**, *284*, 37–40. [CrossRef]
28. Isik, M.; Fernandes, A.M.; Vijayakrishna, K.; Paulis, M.; Mecerreyes, D. Preparation of poly(ionic liquid) nanoparticles and their novel application as flocculants for water purification. *Polym. Chem.* **2016**, *7*, 1668–1674. [CrossRef]
29. Fuerhacker, M.; Haile, T.M.; Kogelnig, D.; Stojanovic, A.; Keppler, B. Application of ionic liquids for the removal of heavy metals from wastewater and activated sludge. *Water Sci. Technol.* **2012**, *65*, 1765–1773. [CrossRef]
30. Mi, H.; Jiang, Z.; Kong, J. Hydrophobic Poly(ionic liquid) for Highly Effective Separation of Methyl Blue and Chromium Ions from Water. *Polymers* **2013**, *5*, 1203–1214. [CrossRef]
31. Atta, A.M.; Al-Lohedan, H.A.; Ezzat, A.O.; Tawfik, A.M.; Hashem, A.I. Synthesis of zinc oxide nanocomposites using poly (ionic liquids) based on quaternary ammonium acrylamidomethyl propane sulfonate for water treatment. *J. Mol. Liq.* **2017**, *236*, 38–47. [CrossRef]
32. Atta, A.M.; Ezzat, A.O.; Hashem, A.I. Synthesis and application of monodisperse hydrophobic magnetite nanoparticles as an oil spill collector using an ionic liquid. *RSC Adv.* **2017**, *7*, 16524–16530. [CrossRef]
33. Atta, A.M.; Ezzat, A.O.; Al-Hussain, S.A.; Al-Lohedan, H.A.; Tawfeek, A.M.; Hashem, A.I. New crosslinked poly (ionic liquid) cryogels for fast removal of methylene blue from waste water. *React. Funct. Polym.* **2018**, *131*, 420–429. [CrossRef]
34. Ma, C.; Laaksonen, A.; Liu, C.; Lu, X.; Ji, X. The peculiar effect of water on ionic liquids and deep eutectic solvents. *Chem. Soc. Rev.* **2018**, *47*, 8685–8720. [CrossRef]
35. Bagheri, M.; Masteri-Farahani, M.; Ghorbani, M. Synthesis and characterization of heteropolytungstate-ionic liquid supported on the surface of silica coated magnetite nanoparticles. *J. Magn. Magn. Mater.* **2013**, *327*, 58–63. [CrossRef]
36. Worldwide, M.I. *Dynamic Light Scattering, Common Terms Defined*; Inform White Paper; Malvern Instruments Limited: Malvern, UK, 2011; pp. 1–6.
37. Lee, C.H.; Park, S.H.; Chung, W.; Kim, J.Y.; Kim, S.H. Preparation and characterization of surface modified silica nanoparticles with organo-silane compounds. *Colloids Surf. A Physicochem. Eng. Asp.* **2011**, *384*, 318–322. [CrossRef]
38. Rosenholm, J.M.; Zhang, J.; Sun, W.; Gu, H. Large-pore mesoporous silica-coated magnetite core-shell nanocomposites and their relevance for biomedical applications. *Microporous Mesoporous Mater.* **2011**, *145*, 14–20. [CrossRef]
39. Itoh, H.; Sugimoto, T. Systematic control of size, shape, structure, and magnetic properties of uniform magnetite and maghemite particles. *J. Colloid Interface Sci.* **2003**, *265*, 283–295. [CrossRef]
40. Atta, A.M.; Al-Lohedan, H.A.; Al-Hussain, S.A. Synthesis of Stabilized Myrrh-Capped Hydrocolloidal Magnetite Nanoparticles. *Molecules* **2014**, *19*, 11263–11278. [CrossRef]
41. Akl, M.A.; Atta, A.M.; Yousef, A.E.F.M.; Alaa, M.I. Characterization of stabilized porous magnetite core-shell nanogel composites based on crosslinked acrylamide/sodium acrylate copolymers. *Polym. Int.* **2013**, *62*, 1667–1677. [CrossRef]
42. Zhang, Y.R.; Su, P.; Huang, J.; Wang, Q.R.; Zhao, B.X. A magnetic nanomaterial modified with poly-lysine for efficient removal of anionic dyes from water. *Chem. Eng. J.* **2015**, *262*, 313–318. [CrossRef]

43. Deng, Y.; Qi, D.; Deng, C.; Zhang, X.; Zhao, D. Superparamagnetic High-Magnetization Microspheres with an Fe_3O_4@SiO_2 Core and Perpendicularly Aligned Mesoporous SiO_2 Shell for Removal of Microcystins. *J. Am. Chem. Soc.* **2008**, *130*, 28–29. [CrossRef] [PubMed]
44. Cheng, J.; Shi, L.; Lu, J. Amino ionic liquids-modified magnetic core/shell nanocomposite as an efficient adsorbent for dye removal. *J. Ind. Eng. Chem.* **2016**, *36*, 206–214. [CrossRef]
45. Saharan, P.; Chaudhary, G.R.; Mehta, S.K.; Umar, A. Removal of water contaminants by iron oxide nanomaterials. *J. Nanosci. Nanotechnol.* **2014**, *14*, 627–643. [CrossRef] [PubMed]
46. Lian, L.; Guo, L.; Guo, C. Adsorption of Congo red from aqueous solutions onto Ca-bentonite. *J. Hazard. Mater.* **2009**, *161*, 126–131. [CrossRef] [PubMed]
47. Xia, C.; Jing, Y.; Jia, Y.; Yue, D.; Ma, J.; Yin, X. Adsorption properties of congo red from aqueous solution on modified hectorite: Kinetic and thermodynamic studies. *Desalination* **2011**, *265*, 81–87. [CrossRef]
48. Weber, T.W.; Chakravorti, R.K. Pore and solid diffusion models for fixed-bed adsorbers. *AIChE J.* **1974**, *20*, 228–238. [CrossRef]
49. Barkakati, P.; Begum, A.; Das, M.L.; Rao, P.G. Adsorptive separation of Ginsenoside from aqueous solution by polymeric resins: Equilibrium, kinetic and thermodynamic studies. *Chem. Eng. J.* **2010**, *161*, 34–45. [CrossRef]
50. Karagoz, S.; Tay, T.; Uçar, S.; Erdem, M. Activated carbons from waste biomass by sulfuric acid activation and their use on methylene blue adsorption. *Bioresour. Technol.* **2008**, *99*, 6214–6222. [CrossRef]
51. Yu, Q.; Deng, S.; Yu, G. Selective removal of perfluorooctane sulfonate from aqueous solution using chitosan-based molecularly imprinted polymer adsorbents. *Water Res.* **2008**, *42*, 3089–3097. [CrossRef]
52. Yan, J.; Huang, Y.; Miao, Y.E.; Tjiu, W.W.; Liu, T. Polydopamine-coated electrospun poly(vinyl alcohol)/poly(acrylic acid) membranes as efficient dye adsorbent with good recyclability. *J. Hazard. Mater.* **2015**, *283*, 730–739. [CrossRef] [PubMed]
53. Belhachemi, M.; Addoun, F. Adsorption of congo red onto activated carbons having different surface properties: Studies of kinetics and adsorption equilibrium. *Desalin. Water Treat.* **2012**, *37*, 122–129. [CrossRef]
54. Madrakian, T.; Afkhami, A.; Ahmadi, M. Adsorption and kinetic studies of seven different organic dyes onto magnetite nanoparticles loaded tea waste and removal of them from wastewater samples. *Spectrochim. Acta Part A Mol. Biomol. Spectrosc.* **2012**, *99*, 102–109. [CrossRef] [PubMed]
55. Wang, L.; Wang, A.Q. Removal of Congo red from aqueous solution using a chitosan/organo-montmorillonite nanocomposite. *J. Chem. Technol. Biotechnol.* **2007**, *82*, 711–720. [CrossRef]
56. Mall, I.; Srivastava, V.C.; Kumar, G.; Mishra, I. Characterization and utilization of mesoporous fertilizer plant waste carbon for adsorptive removal of dyes from aqueous solution. *Colloids Surf. A Physicochem. Eng. Asp.* **2006**, *278*, 175–187. [CrossRef]